Med Biol Eng Comput (2013) 51:741–755
DOI 10.1007/s11517-012-0989-2

ORIGINAL ARTICLE

Energy harvesting through arterial wall deformation: design considerations for a magneto-hydrodynamic generator

Alois Pfenniger · Dominik Obrist · Andreas Stahel · Volker M. Koch · Rolf Vogel

Received: 11 September 2012 / Accepted: 29 October 2012 / Published online: 22 February 2013

Abstract As the complexity of active medical implants increases, the task of embedding a life-long power supply at the time of implantation becomes more challenging. A periodic renewal of the energy source is often required. Human energy harvesting is, therefore, seen as a possible remedy. In this paper, we present a novel idea to harvest energy from the pressure-driven deformation of an artery by the principle of magneto-hydrodynamics. The generator relies on a highly electrically conductive fluid accelerated perpendicularly to a magnetic field by means of an efficient lever arm mechanism. An artery with 10 mm inner diameter is chosen as a potential implantation site and its ability to drive the generator is established. Three analytical models are proposed to investigate the relevant design parameters and to determine the existence of an optimal configuration. The predicted output power reaches 65 μW according to the first two models and 135 μW according to the third model. It is found that the generator, designed as a circular structure encompassing the artery, should not exceed a total volume of 3 cm^3.

Keywords Human energy scavenging · Electromagnetism · Fluid–structure interactions · Arterial pulse propagation · Analytical model

A. Pfenniger (✉) · R. Vogel
ARTORG Center for Biomedical Engineering Research, University of Bern, Murtenstrasse 50, Postfach 44, 3010 Bern, Switzerland
e-mail: alois.pfenniger@artorg.unibe.ch

R. Vogel
e-mail: rolf.vogel@spital.so.ch

A. Pfenniger · A. Stahel · V. M. Koch
Engineering and Information Technology, Bern University of Applied Sciences, Quellgasse 21, 2501 Biel, Switzerland
e-mail: andreas.stahel@bfh.ch

V. M. Koch
e-mail: volker.koch@bfh.ch

D. Obrist
Institute of Fluid Dynamics, ETH Zurich, Sonneggstrasse 3, 8092 Zurich, Switzerland
e-mail: obristd@ethz.ch

R. Vogel
Department of Cardiology, Bern University Hospital, 3010 Bern, Switzerland

R. Vogel
Department of Cardiology, Solothurn Hospitals, 4500 Solothurn, Switzerland

1 Introduction

The last two decades have witnessed the development of medical implants of all kinds, providing more sophisticated functions. At the same time, life expectancy of patients carrying these devices increased. Even if advances in low-power electronics are considerable, certain types of implants need extensive processing power, communication capability or actuation strength, often requiring surgical replacement of the power source, i.e., the battery, after a given time. Human energy harvesting—the conversion of energy derived from any source of the human body mainly into electrical energy—may, therefore, bridge the gap between energy demand and battery capacity/life time.

Energy harvesting from the cardiovascular system, which is a continuous and potent energy source, has been investigated through different approaches: pressure gradients [25, 27, 31], motion of the cardiac muscle [8, 34, 44], arterial wall deformation [23, 24] and blood flow [22].

The work presented in this paper merges two distinct fields: biomechanics of the arteries, in particular arterial pulse propagation, and electro-magnetic (EM) induction, in form of magneto-hydrodynamics (MHD). These two fields are coupled by the motion of the arterial wall, which results from arterial pulse propagation and which is used to cause EM induction.

MHD is the branch of continuum mechanics concerned with the flow of electrically conductive fluids (or ionized gases) in the presence of EM fields [30]. This discipline has been extensively studied [5, 17, 29]. As reported by Branover [5], typical applications for MHD range from pumps (e.g., for cooling of nuclear reactors), propulsion systems (e.g., in spacecrafts), metallurgy (e.g., for control of mixing and heat transfer of molten metal) to generators (e.g., in thermal power plants) and sensors (e.g., blood flow measurement).

A recent attempt to harvest human energy by MHD was reported by Jia et al. [11], who designed a generator to fit in a watch and extract energy from the wrist motion. Energy harvesting in watches is an old technique, but the novelty lies in the chosen transduction mechanism. So far, thermal energy by a thermoelectric generator (e.g., *Seiko Thermic*, Seiko Watch Corporation, Japan) and mechanical energy by a micro EM generator driven by an eccentric weight (e.g., *ETA Autoquartz*, ETA SA Manufacture Horlogère Suisse, Switzerland) were used. As generating principle, Jia et al. studied the motion of an electrically conductive fluid within a magnetic field. In vitro experiments produced an output power of 3.61 μW at 1.4 mV.

To experimentally investigate the feasibility of harvesting energy by MHD from a vessel like the left or right internal thoracic artery (2 mm inner diameter, 40 ml min^{-1} average flow rate), we perfused a 1.1 mm × 3.2 mm × 30 mm channel delimited by two carbon electrodes and two permanent magnets. Our results indicate that using a physiologic saline solution, the generated power remains below the nanowatt range, clearly disqualifying this approach. The main issue is the poor electric conductivity of blood of around 0.65 S m^{-1} at 45 % hematocrit [38]. Of further concern are electrochemical reactions occurring at the electrodes when an electric current flow is allowed. As reported by Tandon et al. [33], charge transfer can occur through three mechanisms: non-Faradaic charging/discharging of the electrochemical double-layer, reversible Faradaic reactions and non-reversible Faradaic reactions. The latter is associated with electrode degradation and harmful by-products and would, therefore, pose a serious threat.

The slow velocity of the arterial wall motion is a major drawback for EM induction [23] such that it is of high interest to accelerate it. We, therefore, propose a novel concept for extracting energy by combining arterial wall deformation with MHD. In the present paper, we define the framework of such a harvester first by assessing the setting in which energy shall be harvested and second by identifying the relevant design parameters through analytical approaches.

2 Methods

2.1 Working principle

The proposed concept makes use of the cyclic expansion and contraction of the arteries to move a highly electrically conductive fluid in a compartment outside an artery. This additional compartment consists of a main chamber (MC) and a buffer chamber (BC) connected by four small channels (Fig. 1). Four permanent magnets (NdFeB grade N52) are arranged around the artery and between these four

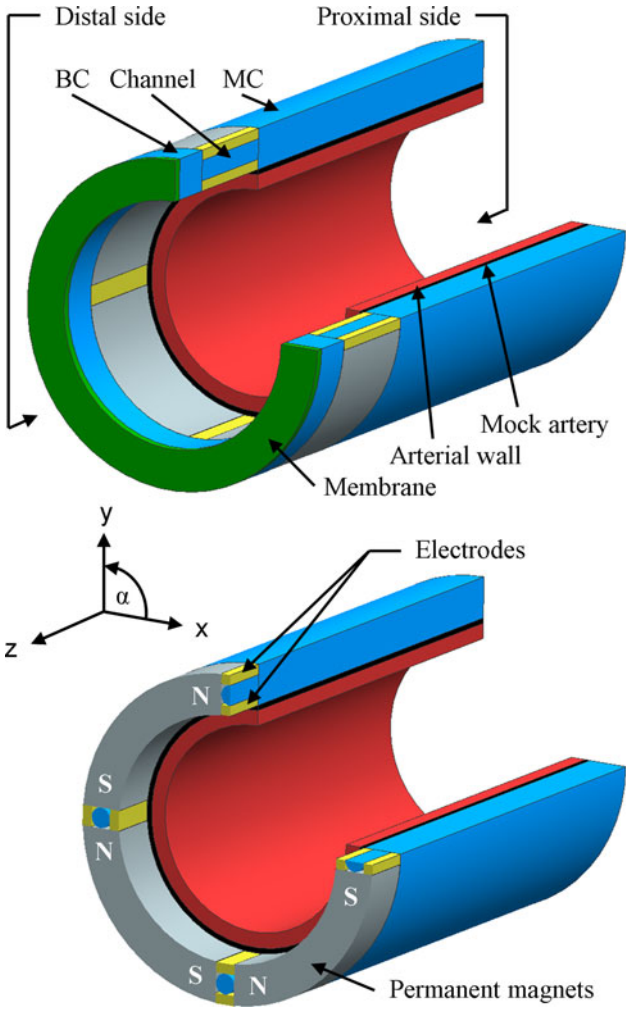

Fig. 1 Schematic representation of the proposed concept. *Blue* MC (large cylinder), BC (small cylinder), channels (small tubes); *red* arterial wall; *black* thin mock artery; *green* membrane; *yellow* electrodes; *grey* permanent magnets. *Bottom panel* section view through channels, permanent magnets and electrodes

channels to create a strong magnetic field perpendicular to the channels' axes. A membrane closes the BC on its distal end, whereas a thin mock artery surrounding the arterial wall closes the MC on its inner wall. The combination of arterial wall and mock artery is later simply referred to as arterial wall. Each channel comprises a pair of electrodes to which a load can be connected.

The working principle is as follows: during systole the arterial wall expands, such that the pressure in the MC becomes higher than in the BC, which leads to a forward flow of the fluid through the channels. To accommodate the resulting volume increase in the BC, the membrane deforms. At end-systole, an amount of fluid has been displaced from the MC to the BC and both the arterial wall and the membrane are deformed. During this process, energy has been extracted by MHD in the channels. During diastole, the pressure in the MC becomes lower than in the BC, leading to a backward flow of the fluid. At end-diastole, the arterial wall and the membrane have recovered their initial shape. Again, energy has been converted by MHD. Over time, the fluid flows back and forth through the channels resulting in an alternating voltage and current through the load. This design is reminiscent of a hydraulic piston, which is driven by the arterial pressure. The slow radial deformation of the artery is concentrated to four tiny cross sections, greatly increasing the velocity. Since a fluid is necessary anyway to obtain the intended lever arm mechanism, it is sensible to use a fluid that also serves as electric conductor.

2.2 Preliminaries

2.2.1 Arterial pressure pulse and arterial wall

An examination of both the arterial pressure pulse and the arterial wall is necessary to evaluate a device harvesting its energy from the pressure-driven deformation of an artery. Equation (1), adapted from Vasava et al. [37], models a typical physiological arterial pressure pulse (in mmHg) as reported by Murgo et al. [19]. To obtain a smooth expression, this piecewise function is approximated by the first 25 terms (this ensures sufficient accuracy) of a Fourier series as seen in (2). The pressure pulse (1) and its frequency spectrum are depicted in Fig. 2.

$$p_{\mathrm{a}}(t) = 80 + \frac{120-80}{2} \times \begin{cases} 0.5 + 0.5\cos(10\pi(t-0.1)), & 0 < t \le 0.1 \\ 1.5 - 0.5\cos(10\pi(t-0.5)), & 0.1 < t \le 0.3 \\ 0.5 + 0.5\cos(5/3\pi(t-0.3)), & 0.3 < t \le 0.9 \end{cases} \quad (1)$$

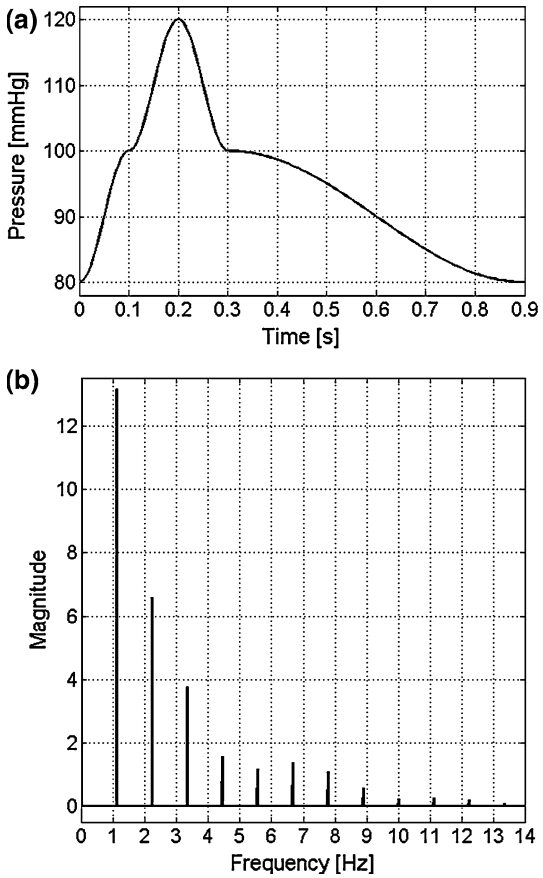

Fig. 2 **a** Physiological pressure pulse (1) with diastolic/systolic pressures of 80 mmHg/120 mmHg. Systole lasts from 0 to 0.3 s and a complete heart cycle takes 0.9 s. **b** Frequency spectrum of the pressure pulse (1)

$$p_{\mathrm{a}}(t) = C + \sum_{n=1}^{12} A_n \cos(\omega_n t) + \sum_{n=1}^{12} B_n \sin(\omega_n t) \quad (2)$$

In a first approximation, we consider the arterial wall as a linear elastic isotropic material, although it is known that the arterial tissue has a nonlinear stress–strain relation [3], behaves viscoelastically [4, 40] and has anisotropic properties [26]. These limitations will be addressed in the discussion in Sect. 4.3.

2.2.2 Energy considerations

A detailed study of an arterial segment's energy balance should precede any attempt to harvest its energy. To this end, we refer to the work by Fung [7], who studied the energy balance over a vessel segment delimited by an inlet and an outlet station. We find that the work done by blood on the arterial wall during systole reads:

$$\int_0^{t_{sys}} p_a(\tau) S(\tau) u_r(\tau) d\tau, \quad (3)$$

where p_a is the arterial blood pressure, S is the surface of contact between blood and the vessel wall and u_r is the radial velocity of the arterial wall. The derivation, containing expressions for S and u_r, can be found in Appendix 1. With this equation at hand, the setting of our energy harvester can be characterized by computing the strain energy in an *undisturbed* arterial segment as a function of time.

2.3 Three analytical models

The device to be evaluated includes fluid–structure interactions—between arterial wall and fluid and between membrane and fluid—as well as magnetic and electric fields (MHD in the channels). The governing laws of MHD can be summarized by the following three equations, expressed for average scalar quantities instead of the usual vector fields [17]:

$$E_{ind} = -w_{mean} B \quad (4)$$

$$J = \sigma_E E_{ind}/2 \quad (5)$$

$$F_L = JB = -w_{mean} \sigma_E B^2/2. \quad (6)$$

Equation (4) establishes the relation between the fluid's mean flow velocity w_{mean}, the magnetic induction B and the induced electric field E_{ind}. Equation (5) expresses Ohm's law in the fluid of electrical conductivity σ_E. The factor ½ arises when matching the source and load resistance. Finally, Eq. (6) models the Lorentz force density F_L resulting from an electric current J through the magnetic induction and opposing the fluid's motion.

Three successive analytical models with increasing level of complexity will be investigated (Table 1). They all rely on the following assumptions and simplifications (a detailed account is provided in Appendix 2):

- the electric power is computed from an averaged rectangular geometry of the electrodes,
- the spatial distribution of the magnetic induction in the channels is approximated by an average value,
- the fluid flow in the MC and BC is modelled by lumped inertial and viscous contributions, which are included in the modelling of the channels,
- the fluid flow in the channels is assumed to be axisymmetric and constant in the axial direction.

The rationale for using three different models follows from two fundamental quantities, the Reynolds and the Womersley [42] number:

- Putting MHD aside, a rough estimation of the Reynolds number in the channels reveals that inertial forces could be important, maybe even dominant. The MHD effect, however, can be understood as an additional damping contribution which may render the inertial forces irrelevant. Therefore, it is of interest to compare a modelling scenario which does not account for inertial forces (model I) with one that does (model II).
- Non-parabolic velocity profiles [42] are expected in the channels due to high Womersley numbers. Therefore, the third approach uses the unsteady momentum equation to account for the shape of the axial velocity profiles, whereas models I and II assume a Poiseuille flow in the channels.

All three models are formulated only for a quarter of the whole geometry because of the symmetry of the studied configuration. We define a cylindrical coordinate system $\{r, \varphi, z\}$ in the channel and a flow velocity vector $\mathbf{u} = \{u, v, w\}^T$.

2.3.1 Model I

The first mathematical model is based on Poiseuille's law [32], which relates the volume flow Q—or the mean flow velocity w_{mean}—to the pressure drop Δp over a vessel segment as a function of the vessel's resistance to flow R:

$$Q(t) = \pi r_{ch}^2 w_{mean}(t) = -\Delta p(t)/R \quad (7)$$

Table 1 Overview of the three models and their relevant features

Equation type	Approach	Velocity profile in channel			Modelling of MC & BC
		$\partial/\partial r\,\mathbf{u}$	$\partial/\partial\varphi\,\mathbf{u}$	$\partial/\partial z\,\mathbf{u}$	
Model I: Poiseuille's law					
First-order ordinary differential equation	Analytical	Parabolic	0	0	Lumped viscous force
Model II: Mass-spring-damper oscillator					
Second-order ordinary differential equation	Analytical	Parabolic	0	0	Lumped viscous and inertial forces
Model III: Van Buskirk's model of the SCC					
Second-order partial integro-differential equation	Analytical[a]	Free	0	0	Lumped viscous and inertial forces

[a] Except for determining the eigenvalues

$$R = \frac{8\mu(l_{ch} + l_a/4)}{\pi r_{ch}^4} + \frac{l_{ch}}{\pi r_{ch}^2}\frac{\sigma_E B^2}{2} \tag{8}$$

Note that R takes also into account the lumped viscous contribution of the fluid flow in the MC (coefficient $l_a/4$; see Appendix 2) and that it comprises an additional term to model the resistance due to MHD, which is derived from (6). A schematic representation of the quantities involved is shown in Fig. 3a. l_{ch} and r_{ch} are the length and the radius of the channel and l_a is the length of the arterial segment. μ is the dynamic viscosity of the fluid. Conservation of mass demands that the volume change on the proximal (ΔV_p) and the distal (ΔV_d) side of the channel due to arterial wall and membrane deformation, respectively, be equal:

$$\Delta V_p(t) = \big(p_a(t) - p_p(t)\big)/K_{aw} = \Delta V_d(t) = (p_d(t) - 0)/K_{me}. \tag{9}$$

K_{aw} is the stiffness of both the arterial wall and the mock artery together and K_{me} the stiffness of the membrane, p_p and p_d are the pressures at the proximal and distal cross sections of the channel, and p_a is the arterial pressure pulse. The pressures are, therefore, related by:

$$p_p(t) = p_a(t) - (K_{aw}/K_{me}) \cdot p_d(t). \tag{10}$$

Poiseuille's law (7) can now be written as:

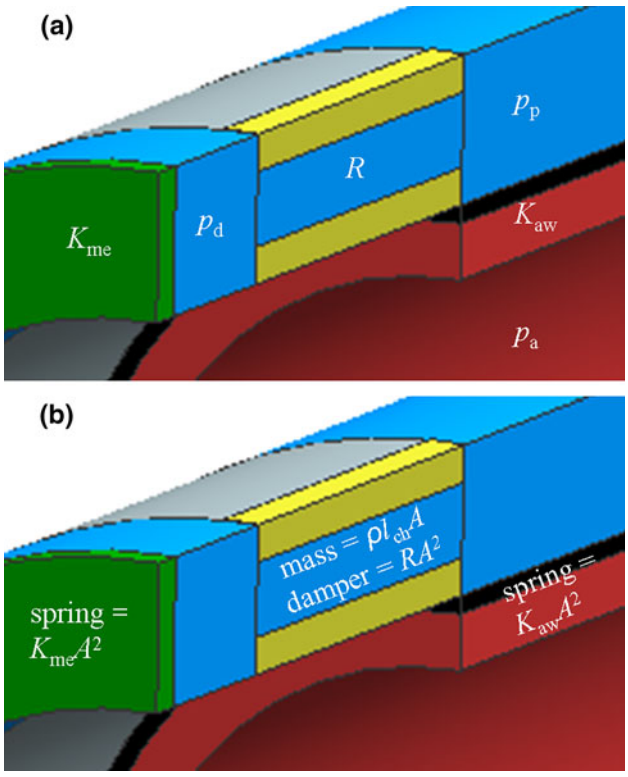

Fig. 3 Close-ups of Fig. 1 with schematic representations of **a** model I (Poiseuille's law) and **b** model II (mass-spring-damper oscillator). $A = \pi r_{ch}^2$

$$p_d'(t)/K_{me} = Q(t) = -\Delta p(t)/R = \big(p_p(t) - p_d(t)\big)/R. \tag{11}$$

Using Eq. (10), we obtain a first-order differential equation for p_d:

$$(R/K_{me}) \cdot p_d'(t) + [(K_{aw} + K_{me})/K_{me}] \cdot p_d(t) = p_a(t). \tag{12}$$

The analytical solution to (12) can be found in Appendix 3.

2.3.2 Model II

Next, we consider the channel as a mass-spring-damper oscillator (Fig. 3b). The fluid (density ρ) in the channel, the viscosity of the fluid and the MHD effect, and the forces exerted by the arterial wall and the membrane represent the mass a, damping b and spring c terms, respectively. As for model I, we point out the lumped inertial and viscous contributions of the fluid flow in the MC (coefficient $l_a/4$ in a and b; see Appendix 2). This leads to a second-order differential equation (13) for the axial fluid displacement s. Its time-derivative (14) gives the mean flow velocity.

$$\begin{aligned} &as''(t) + bs'(t) + cs(t) = \pi r_{ch}^2 p_a(t) \\ &a = \rho(l_{ch} + l_a/4)\pi r_{ch}^2, \\ &b = 8\pi\mu(l_{ch} + l_a/4) + \pi r_{ch}^2 l_{ch}\sigma_E B^2/2, \\ &c = (K_{aw} + K_{me})\pi^2 r_{ch}^4 \end{aligned} \tag{13}$$

$$w_{mean} = \partial s(t)/\partial t \tag{14}$$

From (13), we can derive an expression for the resonance frequency f_{res} of the oscillator:

$$f_{res} = \omega_{res}/2\pi = \sqrt{c/a - b^2/(2a)^2}\Big/2\pi \tag{15}$$

The analytical solution to (13) can be found in Appendix 4.

2.3.3 Model III

The third model is based on the work by Obrist [21] who presents a method to obtain an analytical solution to the Navier–Stokes equations in the context of the human vestibular system (balance organ located in the inner ear). The vestibular system comprises three so-called semicircular canals (SCC), which share many common features with the present energy harvesting concept.

The SCCs are tiny canals filled with a fluid, called the endolymph. Each SCC is closed on one end by a membrane called the cupula. On the other end, the canal expands into a larger chamber filled with endolymph, called utricle. The angular acceleration of the head leads to an inertial force of

the fluid in the SCCs resulting in a deflection of the cupula. The mathematical description of this system was proposed by Van Buskirk et al. [36]:

$$\frac{\partial w(r,t)}{\partial t}+\left(1+\frac{\gamma}{\beta}\right)r_\beta\alpha(t)=-\frac{2\pi K}{\rho\beta r_\beta}\int_0^t\int_0^{r_{ch}} w(\varrho,\tau)\varrho\mathrm{d}\varrho\mathrm{d}\tau + \frac{\mu}{\rho r}\frac{\partial}{\partial r}\left(r\frac{\partial w(r,t)}{\partial r}\right), \tag{16}$$

where β, γ, r_β and r_{ch} define the geometry of the SCC, K is the stiffness of the cupula and $\alpha(t)$ is the head's angular acceleration. From left to right, the terms in (16) denote the axial acceleration of the fluid, the inertia of the fluid in the SCC and in the utricle, the reactive force exerted by the cupula as a result of its deflection and finally the viscous force in the SCC.

The proposed energy harvesting concept also comprises a small canal (the channels) filled with a liquid. Both ends are sealed by the membrane and the arterial wall, respectively. The excitation is now related to the arterial pressure pulse p_a on the arterial wall, leading to a pressure gradient p_a/l_{ch} across the channel. Furthermore, we must take into account the MHD-induced deceleration of the fluid (Eq. 6). Equation (16) can thus be modified as follows:

$$(1+\chi)\frac{\partial w(r,t)}{\partial t} = \frac{p_a(t)}{\rho l_{ch}}-\frac{2\pi(K_{aw}+K_{me})}{\rho l_{ch}}\int_0^t\int_0^{r_{ch}} w(\varrho,\tau)\varrho\mathrm{d}\varrho\mathrm{d}\tau + (1+\chi)\frac{\mu}{\rho r}\frac{\partial}{\partial r}\left(r\frac{\partial w(r,t)}{\partial r}\right)-\frac{\sigma_E B^2}{2\rho}w(r,t) \tag{17}$$

The inertia term was replaced by the arterial pressure pulse, the reactive force is now due to both the arterial wall and the membrane and a damping term was added for the MHD effect. $(1+\chi)$ is a weighting coefficient to account for the lumped inertial and viscous contributions of the fluid flow in the MC (see Appendix 2). Using the non-dimensional variables (denoted by a tilde) $\tilde{r}=r/r_{ch}$, $\tilde{t}=t\mu/\left(\rho r_{ch}^2\right)$ and $\tilde{w}=w/1\,[\mathrm{ms}^{-1}]$ as originally proposed by Van Buskirk, we can rewrite (17) in non-dimensional form:

$$(1+\chi)\frac{\partial\tilde{w}}{\partial\tilde{t}}=\frac{r_{ch}^2 p_a}{\mu l_{ch}}-\varepsilon\int_0^{\tilde{t}}\int_0^1\tilde{w}\varrho\mathrm{d}\varrho\mathrm{d}\tau + (1+\chi)\frac{1}{\tilde{r}}\frac{\partial}{\partial\tilde{r}}\left(\tilde{r}\frac{\partial\tilde{w}}{\partial\tilde{r}}\right)-\zeta\tilde{w} \tag{18}$$

$$\varepsilon=2\pi\rho r_{ch}^6(K_{aw}+K_{me})/(\mu^2 l_{ch}),\qquad \zeta=r_{ch}^2\sigma_E B^2/(2\rho) \tag{19}$$

Doing so, all the geometrical parameters and material properties can be grouped in two non-dimensional coefficients ε and ζ, Eq. (19). We applied the method described by Obrist [21], using an eigenfunction expansion (eigenvalues λ_k) to obtain an analytical solution to (17), in order to derive expressions for the flow velocity as a function of the radial position and for the mean flow velocity:

$$\tilde{w}(\tilde{r},\tilde{t})=\frac{r_{ch}^2}{(1+\chi)\mu l_{ch}}\sum_{k=0}^{\infty}\lambda_k\hat{\tilde{w}}_k(\tilde{r})\int_0^1\hat{\tilde{w}}_k(\tilde{r})\varrho\mathrm{d}\varrho \times\int_{-\infty}^{t}p_a(\tau)e^{-\lambda_k(\tilde{t}-\tau)}\mathrm{d}\tau \tag{20}$$

$$\tilde{w}_{mean}(\tilde{t})=\frac{2r_{ch}^2}{(1+\chi)\mu l_{ch}}\sum_{k=0}^{\infty}\lambda_k\left(\int_0^1\hat{\tilde{w}}_k(\tilde{r})\varrho\mathrm{d}\varrho\right)^2 \times\int_{-\infty}^{t}p_a(\tau)e^{-\lambda_k(\tilde{t}-\tau)}\mathrm{d}\tau \tag{21}$$

While the SCCs are super-critically damped systems, the energy harvesting system may be sub-critically damped (depending on the specific configuration). This leads to a pair of complex conjugate eigenvalues and infinitely many real-valued ones which correspond to highly damped modes. The resonance frequency of the system is obtained from the first pair of complex conjugate eigenvalues:

$$f_{res}=\omega_{res}/2\pi=\mathrm{Im}(\lambda_0)\mu/\left(2\pi r_{ch}^2\rho\right) \tag{22}$$

3 Results

3.1 Arterial strain energy density

Using Eqs. (2) and (3), we compute the strain energy density stored in a deformed arterial wall for a segment with the following diastolic dimensions: $r_{i,dia}=5$ mm; $h_{a,dia}=0.75$ mm. Similar dimensions are typically found in the common iliac arteries (radius: 5.2 mm [2, 10]; wall thickness: 0.76 mm [2]). We use a Young's modulus of 500 kPa [41] and a Poisson's ratio of 0.4 [13]. We find 1.6 mJ cm^{-1} strain energy at peak arterial pressure (120 mmHg at 0.2 s). It reduces to 0.7 mJ cm^{-1} at end-systolic pressure (100 mmHg at 0.3 s).

The presence of a generator around the arterial segment will impair its deformation at the benefit of electric energy production. In other words, by computing the peak strain energy of an *undisturbed* arterial segment, we obtain an upper limit for the output energy of our generator. Since some deformation of the arterial wall is required to drive the generator, this limit is out of reach.

3.2 Design parameters

Various quantities can be analyzed with our analytical models. Here, we focus on the most pertinent ones, i.e., the resonance frequency and the influence of channel radius and length on output electric power. So far, two candidates for the conducting fluid were identified: Mercury and Gallium alloy [11]. The latter outperforms the former with regard to output power due to its noticeably higher electrical conductivity and only slightly higher viscosity and was, therefore, selected for our analysis. K_{aw} was set to 35 GPa m^{-3}, which corresponds to the stiffness of a 2 cm long segment of a common iliac artery ($r_{i,dia} = 5$ mm; $h_{a,dia} = 0.75$ mm) surrounded by a 0.25 mm thick mock artery with the same mechanical properties (see Fig. 1). All three models indicate that the output power would be highest without a membrane (i.e., membrane stiffness $K_{me} = 0$). However, a membrane is required for sealing the BC. We set K_{me} to 19 GPa m^{-3} which describes a membrane with reasonable dimensions made from a material with a low Young's modulus.

All three models were evaluated numerically after 20 cardiac cycles to avoid any transient effects due to the initial conditions. The output electric power was averaged over one cardiac cycle and then quadrupled to account for the symmetries in our modelling approach. The models were evaluated for channel lengths and radii ranging from 0.1 mm to 10 mm and 0.1 to 1 mm, respectively.

3.2.1 Resonance frequency

In contrast to model I, the models II and III are second-order differential equations in time and as such give rise to a resonance frequency (assuming a sub-critical damping). In Fig. 4a, b, the system's resonance frequencies of models II and III are plotted as a function of the channel length l_{ch} and radius r_{ch}. There is a lower threshold below which the system is super-critically damped and no resonance frequency exists. Increasing l_{ch} delays the onset of sub-critical behaviour towards higher r_{ch}. For sufficiently high channel radii, the resonance frequency increases linearly with r_{ch} and is offset by roughly +0.5 Hz for model II (Fig. 4c). Overall, both models are in very good agreement.

3.2.2 Optimal channel length and radius

Figure 5a shows the influence of l_{ch} and r_{ch} on the average output electric power estimated for model I. We observe that the power is highly sensitive on r_{ch} and that this dimension features an optimal value for each channel length. Along the ridge of optimal channel radii, the power increases monotonically with l_{ch} and tends towards a

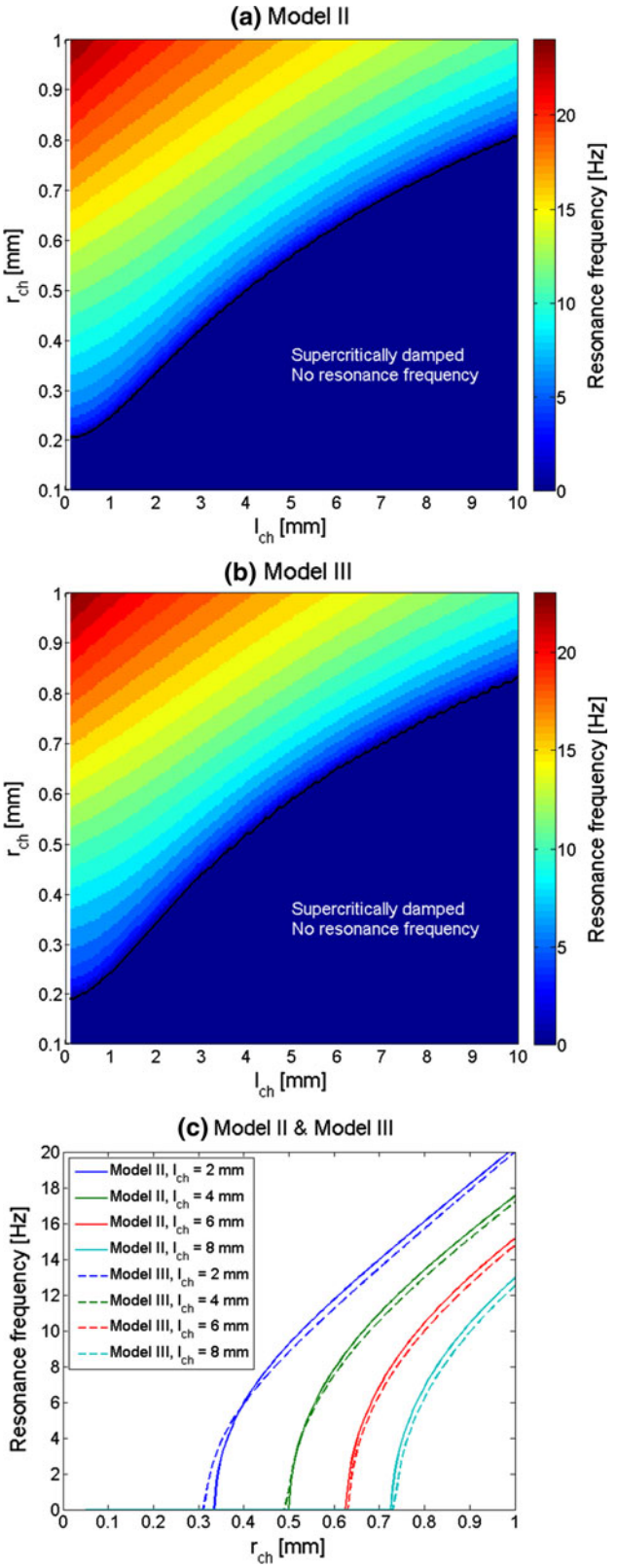

Fig. 4 Resonance frequency of the system according to models II and III for Gallium alloy [11] with $\rho = 5910$ kg m^{-3}, $\mu = 0.00189$ Pa s and $\sigma_E = 6.78$ MS m^{-1}, $B_r = 1.48$ and stiffness $K_{aw} = 35$ GPa m^{-3} and $K_{me} = 19$ GPa m^{-3}

plateau (the gain becomes negligible for $l_{ch} > 10$ mm). For a better visualization, the isolines representing the percentage of output power with regard to the maximum are displayed in white. The maximal power amounts to 64.9 μW and is found for (l_{ch}, r_{ch}) = (10 mm, 0.55 mm), but 90 % output is already obtained for (l_{ch}, r_{ch}) = (3.8 mm, 0.35 mm) and 80 % for (l_{ch}, r_{ch}) = (2.65 mm, 0.29 mm). Figure 5b depicts the same scenario on the basis of model II. The black line denotes the transition from super- to sub-critical damping (cf. Fig. 4a). The maximal power amounts to 68.1 μW and is found for (l_{ch}, r_{ch}) = (10 mm, 0.56 mm). 90 % is already available for (l_{ch}, r_{ch}) = (3.5 mm, 0.34 mm). Although model II indicates a zone where the device could be operated at resonance frequency, the favourable region in terms of output power lies outside. Overall, models I and II are in excellent agreement. In contrast to that, model III (Fig. 5c) behaves fundamentally different as it indicates the presence of an optimal configuration for (l_{ch}, r_{ch}) = (1.6 mm, 0.33 mm). For these dimensions, the system's resonance frequency is 3.2 Hz and the predicted power reaches 134.3 μW. For $l_{ch} = 10$ mm, the optimal r_{ch} is 0.5 mm and the corresponding power is 68.7 μW (i.e., comparable to models I and II).

To exclude that the discrepancy between models I and II on the one hand and model III on the other hand can be attributed to an error in our analytical work, Eqs. (13) and (17) were also integrated numerically. The results proved consistent with the semi-analytical results presented in Fig. 5b, c.

4 Discussion

4.1 A promising energy source

The work done by blood on the arterial wall during systole is stored in the form of strain energy. By neglecting the viscoelastic behaviour of the arterial wall, this strain energy has been slightly overestimated in our computation. In addition, we are aware that by assuming a plane stress approximation (Appendix, Eq. 28), we do not take into account arterial tethering, i.e., the effect of surrounding tissue on the free movement of the arterial wall [9]. An extreme scenario (plane strain approximation with zero longitudinal elongation) resulted in a similar strain energy. Therefore, our approach still provides a reliable estimate for the strain energy despite not being exact, i.e., about 1.6 mJ cm^{-1} in an *undisturbed* common iliac artery at peak systolic strain. Our models indicate that the electric energy converted from arterial pressure by a MHD generator with a 2 cm long MC could amount to 2–4 % of this strain energy (~65 μW according to models I and II and

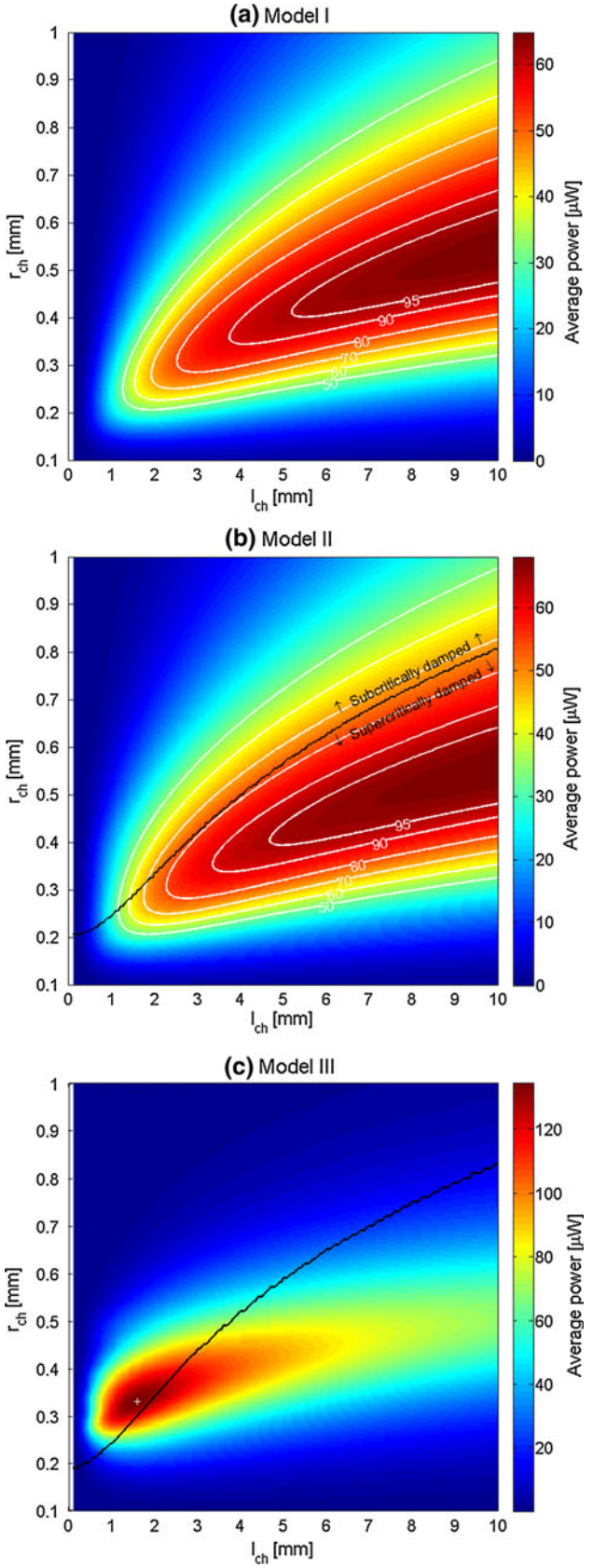

Fig. 5 Average output electric power according to models I, II and III (other specifications as in Fig. 4)

~135 μW according to model III). We point out that this is not to be understood as the conversion efficiency of our generator, which would be determined by assessing the pressure–volume loop in the lumen of the *disturbed* artery. The expected output power in the range of tens of microwatts exceeds existing approaches based on arterial wall deformation by several orders of magnitude (0.006 μW by piezoelectricity [24] and 0.042 μW by electromagnetic induction [23]) and offers sufficient energy to power a pacemaker (<10 μW [43]).

4.2 A device with optimization potential

The results shown in Fig. 4 indicate that the system could be operated at resonance frequency (either the fundamental frequency of the arterial pressure pulse or some of the first harmonics, although their amplitude decreases rapidly as shown in Fig. 2b). At this point, we emphasize that the acceleration experienced by the fluid when flowing from the MC or BC into the narrow channels was not implemented into our models. This effect is expected to delay the onset of resonance towards larger channel radii. Furthermore, it is not clear at this point whether an operation at resonance would be reliable, e.g., due to loss in efficiency when the heart rate is changing.

The excellent agreement for the output power between model I and model II suggests that in the presence of MHD, damping forces largely dominate inertial forces. Therefore, in this particular context, the simpler model I should be preferred. Of particular interest is the comparison between models I and II and model III. They all agree on the existence of an optimal configuration (if we consider the 90 % limit in models I and II as an optimum) but not on its location. To better understand the differences between the models, we investigated model III at Womersley numbers well below 2 which are expected to yield a parabolic velocity profile [42], such that models II and III should be equivalent (MHD was removed from the models to exclude any contribution from this effect). Even under these conditions, however, we did not obtain a parabolic velocity profile with model III. We found that the elastic forces of the arterial wall and the membrane lead to a phase shift between pressure gradient and flow, which may explain the observed distortion of the velocity profile in model III. The same phase shift of course also occurs in model II, but it cannot influence the profile's shape by design. This difference in the velocity profiles appears to be the reason for the different output power in models II and III. Furthermore, these observations suggest that constraining the flow in the channel to a Poiseuille-type velocity profile may be a too strong simplification.

The question remains whether we should trust either models I and II or the more sophisticated model III instead. Because model III is closest to the physical problem in terms of modelling complexity, it should be expected to best reflect the nature of the flow in the channels.

Our results consistently indicate that an appropriate design of our energy harvesting device can be realized with channels having a length of less than 4 mm and a radius of less than 0.4 mm. Adding this to the dimensions of the arterial segment to be exploited (i.e., 20 mm length and 5 mm inner radius), we conclude that the overall size of our device should not exceed 3 cm^3 (artery not included).

4.3 Limitations of our analytical approach

As mentioned in the methods section, several assumptions and simplifications were done to facilitate an analytical approach. On the mechanical side, neither (a) the nonlinear, (b) the viscoelastic nor (c) the anisotropic properties of the arterial tissue were modelled:

(a) In contrast to linear-elastic materials, the stress–strain relation in biological tissues depends on strain itself, i.e., tissue stiffness increases with stretching. The compliance of a femoral artery of normotensive humans decreases by roughly 33 % in its operating range between 80 and 120 mmHg [1]. In our setting, it must be pointed out that the generator around the artery segment is expected to strongly reduce the deformation amplitude. Under these circumstances, the use of a constant Young's modulus is acceptable.

(b) Viscoelasticity produces a phase shift between stress and strain, seen as a hysteresis loop (HL) in the stress–strain diagram. For the carotid artery of a young subject, the energy dissipation ratio—(area within HL)/(area between abscissa and HL + area within HL)—has been determined experimentally as 7.18 % [28] and numerically as 7.8 % [39]. It has been previously investigated whether replacing the viscoelastic artery by an elastic interponate enhances energy production of a generator based on arterial deformation, but no appreciable difference could be observed [23]. Because this effect is apparently of minor importance, it was neglected.

(c) Rezakhaniha et al. [26] showed that both collagen and elastin, which are the main constituents of the arterial wall together with smooth muscle cells, exhibit anisotropic properties. The authors achieved an excellent agreement between theory and inflation–extension experiments by accounting for this behaviour in the modelling of arterial wall mechanics. They

nevertheless mention that their work only reflects the passive properties of the arterial wall, because active contribution of the muscular layer has been neglected. Despite the proven anisotropic character of arteries, we ignored this effect to reduce model complexity.

As detailed in Appendix 2, further limitations related to the electric, magnetic and fluidic parts of the system are the following: the electric power was computed based on an average electrode geometry; the magnetic induction in the channels was approximated by an average value; the fluid flow in the MC and BC was neglected and replaced by average inertial and viscous forces; finally, axisymmetry and translational symmetry were assumed in the channels.

The design, manufacturing, assembling and testing of a prototype as envisioned in Fig. 1 represents a much greater challenge than the preliminary test described in the introduction (two carbon electrodes and two permanent magnets forming a rectangular channel). It is not reasonable to build such a prototype at this stage because the present analysis showed that output power is highly sensitive on the channel radius and length and it is difficult to evaluate how the limitations of our models affect these results. Furthermore, models I and II disagree with model III with respect to the optimal configuration and the corresponding output power. This indicates the need for a more accurate model of our device which could be realized as a FEM simulation overcoming the current limitations.

4.4 Design: perivascular, interponate or intravascular?

Mechanical properties of the arteries vary from subject to subject. Furthermore, arteries become stiffer with age [18]. Other factors that reduce arterial compliance are arterial hypertension, atherosclerosis, diabetes and heart failure [12]. McVeigh et al. [16] reported a significant negative correlation between large artery compliance and age. Based on their findings (invasive blood pressure measurements) in healthy normotensive volunteers, we can derive an average decrease of 52 % in large artery compliance between the age of 20 and 75.

With the configuration envisioned in Fig. 1 (see also Fig. 6a), a stable output power cannot be ensured if the compliance of the target artery is uncertain. As an alternative, the device could be designed as an interponate (Fig. 6b) with known and constant mechanical properties, however, at the cost of a more complex surgical implantation and its complications. If the proposed concept can be sufficiently miniaturized, it could be made deployable and implantable by a catheter intervention. The device could then be expanded at the desired location like a stent. In this case, the device would be located inside the artery

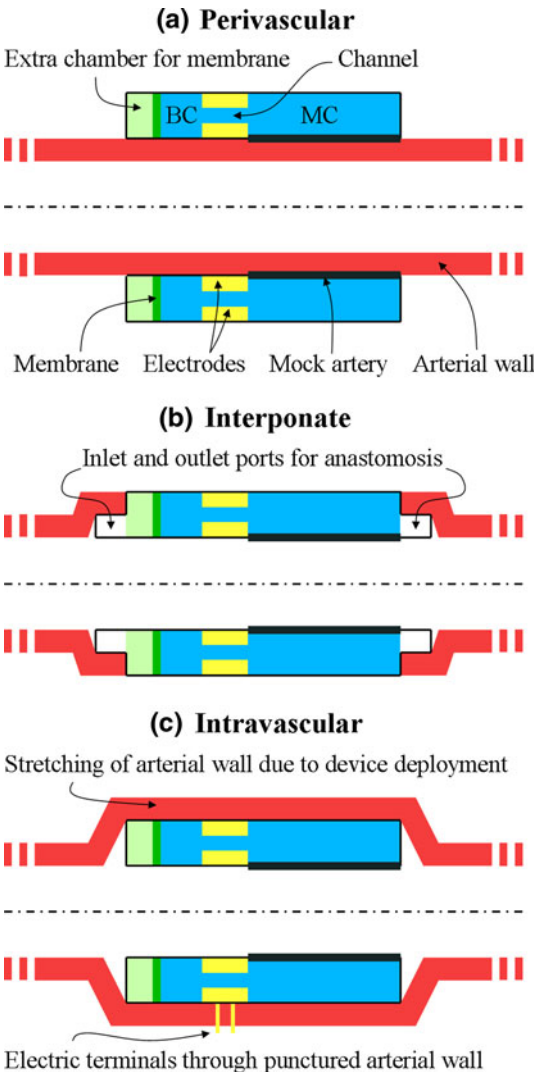

Fig. 6 Schematic representation of three possible designs: **a** perivascular, **b** interponate, **c** intravascular. An extra chamber is added as compared to Fig. 1 to allow the membrane to freely deform despite surrounding structures. In designs **b** and **c**, the mock artery replaces the arterial wall and is designed such that its stiffness equals the stiffness of mock artery and arterial wall together in design **a**. In design **b**, the device comprises inlet and outlet ports for the anastomosis of the target vessel. In design **c**, the stretching of the vessel resulting from the expansion of the device ensures mechanical fixation. The electric power can be made available outside the artery through tiny terminals which puncture the arterial wall during expansion of the device

(Fig. 6c). However, other than the present design, these two approaches are in direct contact with blood.

4.5 Perturbation of the cardiovascular system

The proposed concept alters the mechanical properties of the arterial segment to be exploited. The additional structures placed around the artery induce a compliance

mismatch. The main concern thereby is the disruption in the propagation of the pressure wave. Similar effects have been studied in the context of artery stenting to understand endothelial dysfunction and in-stent restenosis, which are well-known complications of this procedure. Wall shear stress distribution—dictated by the presence of locally irregular flow patterns which are symptomatic of compliance mismatch—is a key concept when it comes to understanding plaque formation [35].

The reflection of pressure waves due to stenting has been studied among others by Nicoud [20]. Assuming an elastic artery and three successive homogeneous segments (pre-stent, stent, post-stent) each having a set of constant area and compliance, Nicoud showed that the coefficient of wave reflexion is proportional to the stent-to-wavelength ratio. Since the wavelength of the arterial pressure wave in the cardiovascular system is typically on the order of a few meters and the length of a stent is a few centimetres, the amount of wave reflexion is expected to be rather small. Based on data obtained from animal experiments, Nicoud concluded that the reflexion coefficient reaches only a few percent. Whether this effect is relevant for the present device and whether it will affect the cardiovascular system must be clarified by further studies.

As stated previously [23], "the artery may not only experience changes of mechanical properties but also undergo biological changes to the physical pressure and foreign body reaction caused by the device. From stenting procedures, we learnt that arteries well comply with the presence of endovascular foreign bodies. However, the biologic activity of the adventitia, i.e., the outer layer of an arterial wall, is much lower than the one of the intima, i.e., the inner layer of an artery, which is in direct contact with an arterial stent. We, therefore, do not expect relevant tissue damage caused by our device. However, minimal inflammatory reactions may occur and induce hardening of the artery, which in turn may affect the performance of our device as mentioned in Sect. 4.4. This would further support a concept as interponate".

5 Conclusion

We presented a novel approach to harvest energy by MHD from arterial wall deformation, which is a mechanism that was shown to deserve attention. The most interesting finding of our analysis is the relatively large output power of the device, expected to feature an optimal configuration at reasonably small dimensions: a MHD generator having a length of 3 cm and adding as little as 2 mm to the radius of the artery could deliver several times the power requirements of a cardiac pacemaker. We plan to implement a full multiphysics FEM simulation to confirm the optimal configuration prior to designing a functional prototype.

Appendix 1

Fung [7] studied the energy balance over a vessel segment delimited by an inlet and an outlet station (denoted below by indices 1 and 2, respectively). If gravitational forces, heat exchange with the surrounding tissues, as well as heat generation due to viscous losses in blood are neglected, the energy balance reads (in a cylindrical coordinate system $\{r, \varphi, z\}$):

$$\int_{A_1} p u_z \mathrm{d}A - \int_{A_2} p u_z \mathrm{d}A + \int_S \mathbf{T}\cdot\mathbf{u}\mathrm{d}A = \int_{A_2} \tfrac{1}{2}\rho\, q^2 u_z \mathrm{d}A - \int_{A_1} \tfrac{1}{2}\rho\, q^2 u_z \mathrm{d}A + \int_S \tfrac{1}{2}\rho\, q^2 u_r \mathrm{d}A + \int_V \partial/\partial t\left(\tfrac{1}{2}\rho q^2\right)\mathrm{d}V \tag{23}$$

$$\mathbf{u} = [u_r\, u_\varphi\, u_z]^T, \qquad \mathbf{T} = [T_r\, T_\varphi\, T_z]^T, \qquad q = \sqrt{u_r^2 + u_\varphi^2 + u_z^2}. \tag{24}$$

A represents the cross section of the vessel, S the surface of contact between blood and the vessel wall and V the volume of the vessel segment. $\mathbf{u}$ is the velocity vector of blood and $\mathbf{T}$ the stress vector acting on the inner surface of the vessel wall. The terms on the left side of (23) stand for the work done on blood by pressure and shear forces, whereas the terms on the right side are related to the kinetic energy of blood [7]. Assuming Poiseuille flow, the velocity component u_φ vanishes due to axisymmetry. Furthermore, u_z vanishes at the wall due to the no-slip boundary condition. Thus, the only rate of work done on the vessel wall is:

$$\int_S \mathbf{T}\cdot\mathbf{u}\mathrm{d}A = \int_S T_r u_r \mathrm{d}A \tag{25}$$

The radial stress component T_r acting on the surface of the vessel wall is the arterial blood pressure p_a. For short segments, it is reasonable to assume a constant arterial pressure. To compute the work done on the vessel wall during systole, Eq. (25) is integrated over time:

$$\int_0^{t_\mathrm{sys}} \int_{S(\tau)} p_\mathrm{a}(\tau) u_r(\tau) \mathrm{d}A \mathrm{d}\tau \tag{26}$$

Next, we assume that u_r can be expressed as a function of p_a. Wall displacement and pressure are related through the average angular stress σ_φ in the arterial wall, as expressed in Laplace's law for a tube [14] (r_i: inner radius of artery; h_a: thickness of arterial wall):

$$\sigma_\varphi = p_\mathrm{a} r_\mathrm{i}/h_\mathrm{a} \tag{27}$$

We further assume a linear elastic isotropic stress–strain relation (see Sect. 2.2.1):

$$\sigma_\varphi = E_a \varepsilon_\varphi = E_a[(r_i + h_a/2) - (r_{i0} + h_{a0}/2)]/(r_{i0} + h_{a0}/2) \tag{28}$$

$$v\varepsilon_\varphi = (l_{a0} + l_a)/l_{a0} = (h_{a0} + h_a)/h_{a0} \tag{29}$$

E_a and v are Young's modulus and Poisson's ratio of the artery, respectively. l_a is the length of the arterial segment. r_{i0}, l_{a0} and h_{a0} are the inner radius of the artery, the length of the arterial segment and the thickness of the arterial wall in absence of any pressure (relaxed state), respectively. By combining (27), (28) and (29), we can derive expressions for the inner radius r_i and the radial velocity u_r as a function of the arterial pressure $p_a(t)$:

$$u_r(t) = \frac{d}{dt} r_i(t) = \frac{d}{dt}\left[-\frac{EFp_a(t) - 8DH + \sqrt{F\left(64D^2 + E^2 F p_a^2(t) - 16DEHp_a(t)\right)}}{32vDE} \right] \tag{30}$$

$$D = E_a h_{a0}, \quad E = (h_{a0} + 2r_{i0}), \quad F = (4 + h_{a0} vE)^2, \quad G = (h_{a0} + 4r_{i0}), \quad H = (4 + vEG)$$

The arterial segment is approximated by a tube of uniform cross-section with the inner surface area being a function of time to account for vessel deformation as a result of pressure change:

$$\begin{aligned} S(t) &= 2\pi r_i(t) l_a(t) \\ &= 2\pi r_i(t) l_{a0}[(1 + v)E - 2v r_i(t)]/(E + h_{a0} v) \end{aligned} \tag{31}$$

Thus we obtain for the work done by blood on the arterial wall during systole:

$$\int_0^{t_{sys}} p_a(\tau) S(\tau) u_r(\tau) d\tau \tag{32}$$

Appendix 2

Our modelling approach relies on the following assumptions and simplifications:

- The useful electric power P in a matched load resistor is computed as:

$$\begin{aligned} P = U \cdot I &= \frac{\int E_{ind} dl}{2} \cdot \int J dA_{el} = \frac{E_{ind}}{2} \cdot \frac{\pi}{2} r_{ch} \cdot J \cdot \frac{\pi}{2} r_{ch} l_{ch} \\ &= w_{mean}^2 \frac{\pi^2}{16} r_{ch}^2 l_{ch} \sigma_E B^2, \end{aligned} \tag{33}$$

where l is the spacing between the electrodes and A_{el} is the electrodes' area. Since the channels have a circular cross section, we take l as the average channel height ($\pi/2 \cdot r_{ch}$) and A_{el} as the average channel width ($\pi/2 \cdot r_{ch}$) times the channel length l_{ch} (Fig. 7a). r_{ch} is the channel radius.

- An average value for the magnetic induction B between two magnetic poles was estimated by the laws of magnetic circuits. B depends on the remanent magnetic induction B_r of the permanent magnets (length l_m, pole area A_m) as well as on the dimensions of the air gap between two poles, i.e., on the channel length l_{ch} and the channel radius r_{ch}. To account for fringing, which becomes relevant when the length of the air gap l_g is of same magnitude as A_m, the area of the air gap A_g was corrected empirically as suggested by Matsch [15] (Fig. 7b):

$$B(r_{ch}, l_{ch}) = \frac{B_r}{A_g(r_{ch}, l_{ch})/A_m(l_{ch}) + l_g(r_{ch})/l_m(r_{ch})} \tag{34}$$

- Our device uses a lever arm mechanism to accelerate the fluid flow in the channels. Thus, we expect that the flow velocity and the related pressure drop will be high in the channels but irrelevant in the MC and the BC. Based on this assumption, the fluid *flow* in the MC and the BC was neglected and the system was reduced to the arterial wall, the channels and the membrane. The arterial wall is virtually located at the proximal end of the channels and the membrane at the distal end. Nevertheless, we realized that this simplification would not do justice to the very important fluid *mass* in the MC compared to the tiny fluid mass in the channels. We, therefore, derived an additional inertial force from the average acceleration experienced by the fluid in the MC (Fig. 7c). We found that this inertial force can be modelled by extending the channels by a fixed length equalling a quarter of the MC length (i.e., $l_a/4$). We decided to also consider the viscous force arising from this extended channel length.
- Neither the magnetic induction B, the induced electric field E_{ind} nor the electric current density J are constant over the channel's cross section (B is location dependent between two magnetic poles, E_{ind} is a function of the flow velocity and J depends on E_{ind} and on the electrode geometry). We easily conclude that the Lorentz force's magnitude is not uniform over the channel's cross section. Thus, in

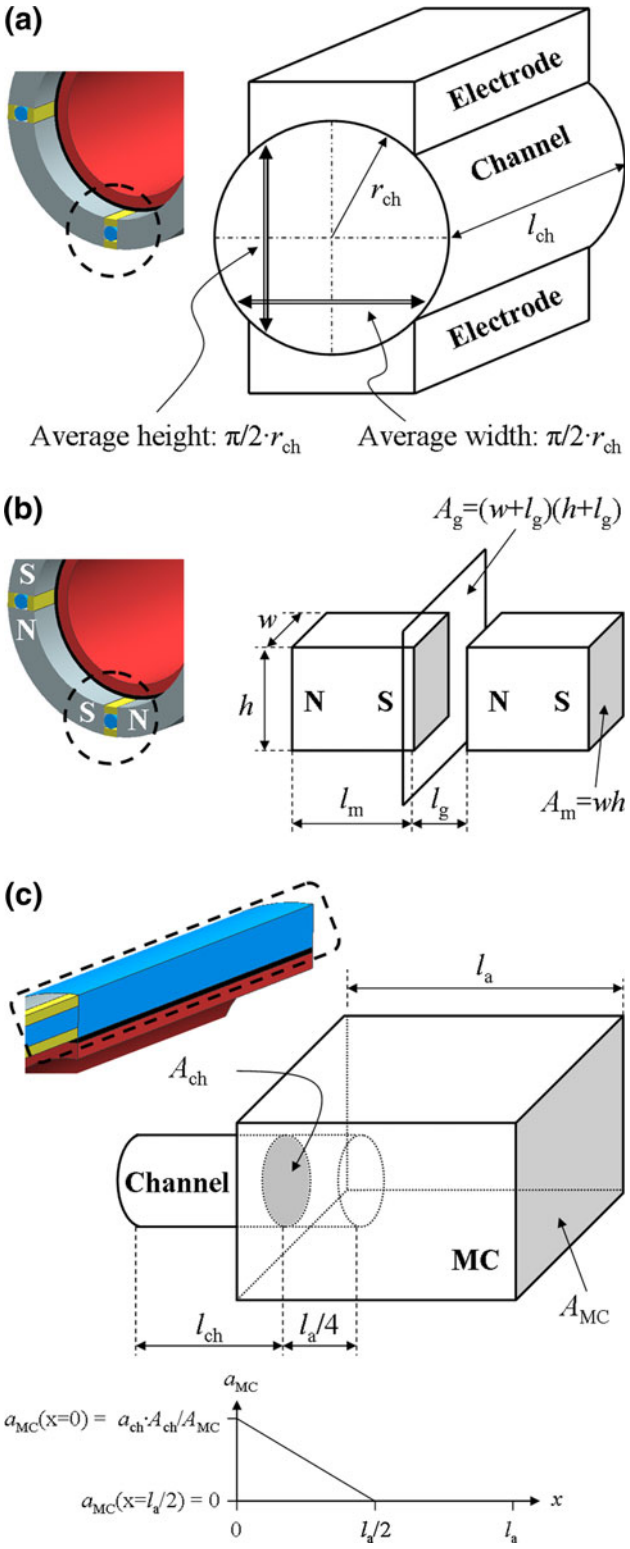

◀ **Fig. 7** Close-ups of Fig. 1: **a** explanation of "average height" and "average width" used to compute the output electric power; **b** correction for fringing at air gap between two magnets: the air gap area A_g is corrected by adding the gap length l_g to each dimension [15]; **c** fluid flow in MC approximated by average inertial and viscous forces: a_{ch} and a_{MC} denote the average acceleration of the fluid in the channel and the MC, respectively. It is assumed that a_{MC} equals a_{ch} times the ratio of the channel cross section A_{ch} to the MC cross section A_{MC} at the MC outlet ($x = 0$) and reaches zero at $x = l_a/2$. This corresponds to extending l_{ch} by a factor of $l_a/4$

the presence of MHD, the fluid flow in the channels is not axisymmetric. For simplicity, we nevertheless assumed an axisymmetric flow profile in our models.

- Based on the work of Fargie and Martin [6], we can deduce that the entry region, in which the laminar flow develops, spans the whole channels at peak forward and peak backward flow. Nevertheless, we neglect this effect and assume translational symmetry in the channels. Similar simplifications are often applied in cardiovascular engineering due to the complexity of the arterial tree with its many branchings.

Appendix 3

The solution to (12) is the sum of a homogeneous and inhomogeneous part:

$$p_d(t) = k \cdot p_{d\_h}(t) + p_{d\_i}(t) \tag{35}$$

$$p_{d\_h}(t) = e^{-\frac{K_{aw}+K_{me}}{R} \cdot t} \tag{36}$$

$$\begin{aligned} p_{d\_i}(t) = {} & [K_{me}/(K_{aw}+K_{me})] \cdot C \\ & + \sum_{n=1}^{12} (a_{na}\cos(\omega_n t) + a_{nb}\sin(\omega_n t)) \\ & + \sum_{n=1}^{12} (b_{na}\cos(\omega_n t) + b_{nb}\sin(\omega_n t)) \end{aligned} \tag{37}$$

where

$$a_{na} = \frac{A_n K_{me}(K_{aw}+K_{me})}{(K_{aw}+K_{me})^2 + R^2\omega_n^2}, \quad a_{nb} = \frac{A_n K_{me} R\omega_n}{(K_{aw}+K_{me})^2 + R^2\omega_n^2}$$
$$b_{na} = \frac{-B_n K_{me} R\omega_n}{(K_{aw}+K_{me})^2 + R^2\omega_n^2}, \quad b_{nb} = \frac{B_n K_{me}(K_{aw}+K_{me})}{(K_{aw}+K_{me})^2 + R^2\omega_n^2} \tag{38}$$

The coefficient k is obtained from the initial condition $p_d(t = 0) = 0$:

$$k = -p_{d\_i}(0)/p_{d\_h}(0) = -p_{d\_i}(0) \tag{39}$$

Appendix 4

Solving the homogeneous and inhomogeneous part of equation (13), one obtains:

$$s(t) = s_h(t) + s_i(t) \tag{40}$$

$$s_{\mathrm{h}}(t) = e^{-\frac{b}{2a}t} \cdot (k_1 \cos(\omega_{\mathrm{res}} t) + k_2 \sin(\omega_{\mathrm{res}} t)) \tag{41}$$

$$s_{\mathrm{i}}(t) = \left(\pi r_{\mathrm{ch}}^2 / c\right) \cdot C + \sum_{n=1}^{12} \left(a_{n\mathrm{a}} \cos(\omega_n t) + a_{n\mathrm{b}} \sin(\omega_n t)\right) + \sum_{n=1}^{12} \left(b_{n\mathrm{a}} \cos(\omega_n t) + b_{n\mathrm{b}} \sin(\omega_n t)\right) \tag{42}$$

where

$$a_{n\mathrm{a}} = \frac{A_n \pi r_{\mathrm{ch}}^2 \left(c - a\omega_n^2\right)}{\psi}, \quad a_{n\mathrm{b}} = \frac{A_n \pi r_{\mathrm{ch}}^2 b \omega_n}{\psi},$$
$$b_{n\mathrm{a}} = \frac{-B_n \pi r_{\mathrm{ch}}^2 b \omega_n}{\psi}, \quad b_{n\mathrm{b}} = \frac{B_n \pi r_{\mathrm{ch}}^2 \left(c - a\omega_n^2\right)}{\psi} \tag{43}$$
$$\psi = c^2 + b^2\omega_n^2 - 2ac\omega_n^2 + a^2\omega_n^4$$

The coefficients k_1 and k_2 are obtained from the initial conditions $s(t = 0) = 0$ and $s'(t = 0) = 0$:

$$k_1 = -s_{\mathrm{i}}(0), \quad k_2 = (k_1/\omega_{\mathrm{res}}) \cdot b/(2a) - s_{\mathrm{i}}'(0)/\omega_{\mathrm{res}} \tag{44}$$

References

1. Armentano R, Megnien JL, Simon A, Bellenfant F, Barra J, Levenson J (1995) Effects of hypertension on viscoelasticity of carotid and femoral arteries in humans. Hypertension 26:48–54
2. Avolio AP (1980) Multi-branched model of the human arterial system. Med Biol Eng Comput 18:709–718
3. Bergel DH (1960) The static elastic properties of the arterial wall. J Physiol 156:445–457
4. Bergel DH (1960) The dynamic elastic properties of the arterial wall. J Physiol 156:458–469
5. Branover H (1978) Magnetohydrodynamic Flow in Ducts. Israel Universities Press, Jerusalem
6. Fargie D, Martin BW (1971) Developing laminar flow in a pipe of circular cross-section. Proc R Soc Lond A 321:461–476
7. Fung YC (1997) Biomechanics: circulation, 2nd edn. Springer, New York
8. Goto H, Sugiura T, Harada Y, Kazui T (1999) Feasibility of using the automatic generating system for quartz watches as a leadless pacemaker power source. Med Biol Eng Comput 37:377–380
9. Hodis A, Zamir M (2009) Arterial wall tethering as a distant boundary condition. Phys Rev E 80:051913
10. Horejs D, Gilbert PM, Burstein S, Vogelzang RL (1988) Normal aortoiliac diameters by CT. J Comput Assisted Tomogr 12:602–603
11. Jia D, Liu J, Zhou Y (2009) Harvesting human kinematical energy based on liquid metal magnetohydrodynamics. Phys Lett A 373:1305–1309
12. Kuecherer HF, Just A, Kirchheim H (2000) Evaluation of aortic compliance in humans. Am J Physiol Heart Circ Physiol 278:H11411–H11413
13. Lees C, Vincent JF, Hillerton JE (1991) Poisson's ratio in skin. Biomed Mater Eng 1:19–23
14. Levy MN, Pappano AJ (2007) Cardiovascular physiology, 9th edn. Mosby Elsevier, Philadelphia
15. Matsch LW (1964) Capacitors, magnetic circuits, and transformers. Prentice-Hall, Englewood Cliffs
16. McVeigh GE, Bratteli CW, Morgan DJ, Alinder CM, Glasser SP, Finkelstein SM, Cohn JN (1999) Age-related abnormalities in arterial compliance identified by pressure pulse contour analysis: aging and arterial compliance. Hypertension 33:1392–1398
17. Messerle HK (1995) Magneto-hydro-dynamic electrical power generation. Wiley, Chichester
18. Mohiaddin RH, Underwood SR, Bogren HG, Firmin DN, Klipstein RH, Rees RS, Longmore DB (1989) Regional aortic compliance studied by magnetic resonance imaging: the effects of age, training, and coronary artery disease. Br Heart J 62:90–96
19. Murgo JP, Westerhof N, Giolma JP, Altobelli SA (1980) Aortic input impedance in normal man: relationship to pressure wave forms. Circulation 62:105–116
20. Nicoud F (2002) Hemodynamic changes induced by stenting in elastic arteries. Center for turbulence research, Annual Research Briefs, pp 335–347
21. Obrist D (2008) Fluidmechanics of semicircular canals—revisited. Z Angew Math Phys 59:475–497
22. Pfenniger A, Koch VM, Vogel R (2011) Human energy harvesting by intravascular turbine generators. In: Proceedings of the 6th international conference on microtechnologies in medicine and biology (MMB 2011), Lucerne, pp 82–83
23. Pfenniger A, Wickramarathna LN, Vogel R, Koch VM (2013) Design and realization of an energy harvester using pulsating arterial pressure. Med Eng Phys. doi:10.1016/j.medengphy.2013.01.001
24. Potkay JA, Brooks K (2008) An arterial cuff energy scavenger for implanted microsystems. In: The 2nd international conference on bioinformatics and biomedical engineering (ICBBE 2008), pp 1580–1583
25. Ramsay MJ, Clark WW (2001) Piezoelectric energy harvesting for bio MEMS applications. Proc SPIE 4332:429–438
26. Rezakhaniha R, Fonck E, Genoud C, Stergiopulos N (2011) Role of elastin anisotropy in structural strain energy functions of arterial tissue. Biomech Model Mechanobiol 10:599–611
27. Roberts P, Stanley G, Morgan JM (2008) Abstract 2165: harvesting the energy of cardiac motion to power a pacemaker. Circulation 118:679–680
28. Shau YW, Wang CL, Shieh JY, Hsu TC (1999) Noninvasive assessment of the viscoelasticity of peripheral arteries. Ultrasound Med Biol 25:1377–1388
29. Shercliff JA (1962) The theory of electromagnetic flow-measurement. Cambridge University Press, Cambridge
30. Snarski SR, Kasper RG, Bruon AB (2004) Device for electromagnetohydrodynamic (EMHD) energy harvesting. Proc SPIE 5417:147–161
31. Sohn JW, Choi SB, Lee DY (2005) An investigation on piezoelectric energy harvesting for MEMS power sources. Proc IMechE Part C J Mech Eng Sci 219(4):429–436
32. Sutera SP, Skalak R (1993) The history of Poiseuille's law. Annu Rev Fluid Mech 25:1–19
33. Tandon N, Cannizzaro C, Chao PH, Maidhof R, Marsano A, Au HT, Radisic M, Vunjak-Novakovic G (2009) Electrical stimulation systems for cardiac tissue engineering. Nat Protoc 4:155–173
34. Tashiro R, Kabei N, Katayama K, Tsuboi F, Tsuchiya K (2002) Development of an electrostatic generator for a cardiac pacemaker that harnesses the ventricular wall motion. J Artif Org 5:239–245
35. Tortoreillo A, Pedrizzetti G (2004) Flow-tissue interaction with compliance mismatch in a model stented artery. J Biomech 37:1–11
36. Van Buskirk WC, Watts RG, Liu YK (1976) The fluid mechanics of the semicircular canals. J Fluid Mech 78:87–98
37. Vasava P, Jalali P, Dabagh M (2009). Pulsatile blood flow simulations in aortic arch: effects of blood pressure and the geometry of arch on wall shear stress. In: Proceedings of the 4th European

conference of the international federation for medical and biological engineering (IFMBE 2009), vol. 22, pp 1926–1929
38. Visser KR (1992) Electric conductivity of stationary and flowing human blood at low frequencies. Med Biol Eng Comput 30:636–640
39. Warriner RK, Johnston KW, Cobbold RS (2008) A viscoelastic model of arterial wall motion in pulsatile flow: implications for Doppler ultrasound clutter assessment. Physiol Meas 29:157–159
40. Westerhofy N, Noordergraaf A (1970) Arterial viscoelasticity: a generalized model. J Biomech 3:357–379
41. Westerhof N, Stergiopulos N, Noble MI (2005) Snapshots of hemodynamics: an aid for clinical research and graduate education. Springer Science + Business Media, Boston
42. Womersley JR (1955) Method for the calculation of velocity, rate of flow and viscous drag in arteries when the pressure gradient is known. J Physiol 127:553–563
43. Wong LS, Hossain S, Ta A, Edvinsson J, Rivas DH, Nääs H (2004) A very low-power CMOS mixed-signal IC for implantable pacemaker applications. IEEE J Solid-St Circ 39:2446–2456
44. Zurbuchen A, Pfenniger A, Stahel A, Stoeck CT, Vandenberghe S, Koch VM, Vogel R (2013) Energy harvesting from the beating heart by a mass imbalance oscillation generator. Ann Biomed Eng 44(1):131–141